Journal of Computational Physics **152,** 642–663 (1999)
Article ID jcph.1999.6257, available online at http://www.idealibrary.com on IDEAL®

A Lattice Boltzmann Scheme for Incompressible Multiphase Flow and Its Application in Simulation of Rayleigh–Taylor Instability[1]

Xiaoyi He, Shiyi Chen, and Raoyang Zhang

Los Alamos National Laboratory, Los Alamos, New Mexico 87545

Received August 10, 1998; revised February 8, 1999

In this paper, we propose a new lattice Boltzmann scheme for simulation of multiphase flow in the nearly incompressible limit. The new scheme simulates fluid flows based on distribution functions. The interfacial dynamics, such as phase segregation and surface tension, are modeled by incorporating molecular interactions. The lattice Boltzmann equations are derived from the continuous Boltzmann equation with appropriate approximations suitable for incompressible flow. The numerical stability is improved by reducing the effect of numerical errors in calculation of molecular interactions. An index function is used to track interfaces between different phases. Simulations of the two-dimensional Rayleigh–Taylor instability yield satisfactory results. The interface thickness is maintained at 3–4 grid spacings throughout simulations without artificial reconstruction steps.

I. INTRODUCTION

Since its precursor—the lattice gas automaton (LGA)—was proposed ten years ago as a useful computational fluid dynamics (CFD) technique [1], the lattice Boltzmann method (LBM) has emerged as a promising approach for simulation of multiphase flow (for review, see [2, 3]). Unlike traditional CFD methods which solve macroscopic equations, the LBM simulates fluid flow based on microscopic models or mesoscopic kinetic equations. This intrinsic feature enables the LBM to incorporate easily many essential physics at microscopic or mesoscopic level. The phase segregation and interfacial dynamics, which are essential in multiphase flow and are difficult to handle by traditional approaches, can be simulated in the lattice Boltzmann method by incorporating intermolecular interactions.

Several LBM models for simulation of multiphase flow have been proposed in the past several years. The first LBM multiphase model was proposed by Gunstensen *et al.* [4]

[1]This research is supported by the Department of Energy under Contract W-7405-ENG-36.

0021-9991/99 $30.00

based on a two-component LGA model [5]. Later, Grunau *et al.* [6] modified this model to allow variations of density and viscosity. In these models, red and blue particle distribution functions were introduced to mimic two different fluids. To maintain interfaces and to separate different phases, a "re-color" step was introduced to force colored fluids to move toward fluids with the same colors. The second LBM multiphase model by Shan and Chen [7] used a concept of the microscopic interactions between particles. An interparticle potential was introduced to model the phase segregation and surface tension. The third LBM model proposed by Swift *et al.* [8] used the free-energy approach. In their model, the equilibrium distribution was modified so that the pressure tensor was consistent with the tensor derived from the free-energy function of non-uniform fluids.

Although each of the above LBM multiphase models was built on different physical pictures and each has a quite different appearance, a recent study by He *et al.* [9] showed that all of them have an origin in the kinetic theory. To be specific, all these models can be derived by discretizing the continuous Boltzmann equation with certain approximations. Some of these approximations turn out to be unphysical and lead to certain unsatisfactory features, such as the spurious current around interfaces and the lack of Galilean invariance. He *et al.* further suggested that an improved LBM scheme for multiphase flow can be derived by systematically removing these unphysical approximations.

In this paper, we propose a new lattice Boltzmann scheme for simulation of multiphase flow in the incompressible limit. The new scheme simulates fluid flows based on distribution functions. The evolution equations for these distributions are derived from the continuous Boltzmann equation with appropriate approximations for incompressible flows. The interfacial dynamics are modeled by incorporating molecular interactions. A pressure distribution function is introduced to replace the single-particle density distribution function. Consequently, the numerical stability of the scheme can be improved by reducing the effect of numerical errors in calculation of molecular interactions. An index function is used to track interfaces between different phases.

The past several years have witnessed numerous efforts to apply the lattice Boltzmann method to multiphase flows. Two fundamental interfacial dynamics, the Laplace law and the dispersion law in capillary waves, have been verified [6, 8, 10]. Other applications include simulations of the spinodal decomposition [11, 12] and multiphase flows through porous media [13]. These works either focused on simple problems or lacked quantitative comparisons with benchmark studies. The accuracy and efficiency of the LBM models in simulation of multiphase flows remain to be explored. It is the purpose of this paper to fill this gap. We will use the Rayleigh–Taylor instability as our test case.

There are several reasons for us to choose the Rayleigh–Taylor instability as our benchmark problem. First, the Rayleigh–Taylor instability is of great significance in both fundamental research and practical applications. At late stages, the flow involves turbulent mixing—a ubiquitous but poorly understood phenomenon. Our study will provide more insight into this classical multiphase flow problem. Second, the Rayleigh–Taylor instability provides enough complexities to challenge the capability of our scheme. Beyond the initial stage, the Rayleigh–Taylor instability exhibits strong non-linearity which is associated with the growth of the secondary Kelvin–Helmholtz instability. The instability evolving from a random initial perturbation exhibits an even more complicated pattern. The success in simulating such a complicated multiphase flow problem will bring great confidence for future applications of the lattice Boltzmann method. Finally, there are copious theoretical

studies and numerical simulations on the Rayleigh–Taylor instability in literature. We can use these data to quantify the accuracy of our scheme.

The rest of the paper is organized as follows: In Section II, the continuous Boltzmann equation for non-ideal fluids will be modified for incompressible flow. In Section III, a new lattice Boltzmann multiphase model is derived by discretizing the continuous kinetic equation. Section IV presents numerical simulations of the two-dimensional Rayleigh-Taylor instability. The results are compared with the theoretical prediction and other computational results. A brief conclusion is given in Section V.

II. BOLTZMANN EQUATION FOR INCOMPRESSIBLE MULTIPHASE FLOW

A. General Theories

It is well known in kinetic theory that fluid flow can be described by the Boltzmann equation. By incorporating the intermolecular interaction force, we can obtain the Boltzmann equation for non-ideal fluids [9],

$$\frac{Df}{Dt} \equiv \frac{\partial f}{\partial t} + \boldsymbol{\xi} \cdot \nabla f = -\frac{f - f^{\mathrm{eq}}}{\lambda} + \frac{(\boldsymbol{\xi} - \mathbf{u}) \cdot (\mathbf{F} + \mathbf{G})}{\rho RT} f^{\mathrm{eq}}, \tag{1}$$

where f is the single particle density distribution function in the phase space, $\boldsymbol{\xi}$ is the microscopic velocity, $\mathbf{G}$ is the gravity, R is the gas constant, and $\mathbf{F}$ is the effective molecular interaction force. In Eq. (1), we have used the single-relaxation-time BGK model [14] for the full collision term and λ is the relaxation time. The equilibrium distribution satisfies the Maxwellian distribution

$$f^{\mathrm{eq}} = \frac{\rho}{(2\pi RT)^{D/2}} \exp\left[-\frac{(\boldsymbol{\xi} - \mathbf{u})^2}{2RT}\right], \tag{2}$$

where D is the dimension of the space. The macroscopic density, ρ, velocity, $\mathbf{u}$, and temperature, T, are calculated as the moments of the distribution function:

$$\rho = \int f \, d\boldsymbol{\xi}, \tag{3}$$

$$\rho \mathbf{u} = \int \boldsymbol{\xi} f \, d\boldsymbol{\xi}, \tag{4}$$

$$\frac{D}{2} \rho RT = \int \frac{(\boldsymbol{\xi} - \mathbf{u})^2}{2} f \, d\boldsymbol{\xi}. \tag{5}$$

In this study, we will only focus on the hydrodynamics of multiphase flow and assume the temperature is constant. Thermal multiphase flow will be postponed to future studies.

Using the mean-field approximation for intermolecular attraction [15] and following the treatment of the exclusion-volume effect by Enskog (cf. Chap. 16 in Ref. [16]), the effective molecular interaction force can be expressed as

$$\mathbf{F} = \rho \nabla (2a\rho + \kappa \nabla^2 \rho) - b\rho^2 RT \chi \nabla \ln(\rho^2 \chi), \tag{6}$$

where the first term comes from the intermolecular attraction and the second term comes from the exclusion-volume effect. The parameters a and κ are related to the intermolecular

pair-wise potential, u_{attr},

$$a = -\frac{1}{2}\int_{r>\sigma} u_{\text{attr}}(r)\, d\mathbf{r}, \tag{7}$$

$$\kappa = -\frac{1}{6}\int_{r>\sigma} r^2 u_{\text{attr}}(r)\, d\mathbf{r}, \tag{8}$$

where σ is the effective diameter of a molecule; $b = 2\pi\sigma^3/3m$ where m is the mass of a single molecule; and χ is the increase in collision probability due to the increase in fluid density, which has the following virial expansion form:

$$\chi(\rho) = 1 + \frac{5}{8}b\rho + 0.2869(b\rho)^2 + 0.1103(b\rho)^3 + \cdots. \tag{9}$$

The above intermolecular force can also be regrouped into a simpler form,

$$\mathbf{F} = -\nabla\psi + \mathbf{F}_{\text{s}}, \tag{10}$$

where $\mathbf{F}_{\text{s}} = \kappa\rho\nabla\nabla^2\rho$ represents the force associated with surface tension (the parameter κ determines the strength of surface tension), and ψ is a function of the density:

$$\psi(\rho) = b\rho^2 RT\chi - a\rho^2. \tag{11}$$

Notice that $\psi(\rho)$ is related to the pressure by $\psi(\rho) = p - \rho RT$, and the pressure satisfies the following equation of state:

$$p = \rho RT(1 + b\rho\chi) - a\rho^2. \tag{12}$$

The first term in Eq. (10), which in turn depends on the equation of state, plays a key role in phase segregation. At a high temperature, the attraction among molecules is weak and the random motion of molecules is dominant. Therefore, a fluid can only exist in a single phase. Once the temperature is reduced below a critical value, the molecular attraction becomes strong enough to induce phase segregation. In the p–V–T diagram, the isothermal at this state is characterized by a supernodal curve (Fig. 1). For a given pressure, there exist three possible solutions of density. Two of them (points A and E) represent the gas and liquid phases and can be found using Maxwell's equal-area rule. The intermediate root (point C) lies on a portion of the supernodal curve that is mechanically unstable ($dp/dV > 0$). It is this unstable portion that induces phase segregation. For fluids originally in two different phases, this unstable state keeps the phases separated and warrants the sharp interface.

The specific value of the critical temperature depends on the equation of state. For the van der Waals equation of state,

$$p = \frac{\rho RT}{1 - b\rho} - a\rho^2, \tag{13}$$

the critical temperature $T_{\text{c}} = 8a/27bR$. For the Carnahan–Starling equation of state [17],

$$p = \rho RT\frac{1 + b\rho/4 + (b\rho/4)^2 - (b\rho/4)^3}{(1 - b\rho/4)^3} - a\rho^2, \tag{14}$$

the critical temperature $T_{\text{c}} = 0.3773a/bR$.

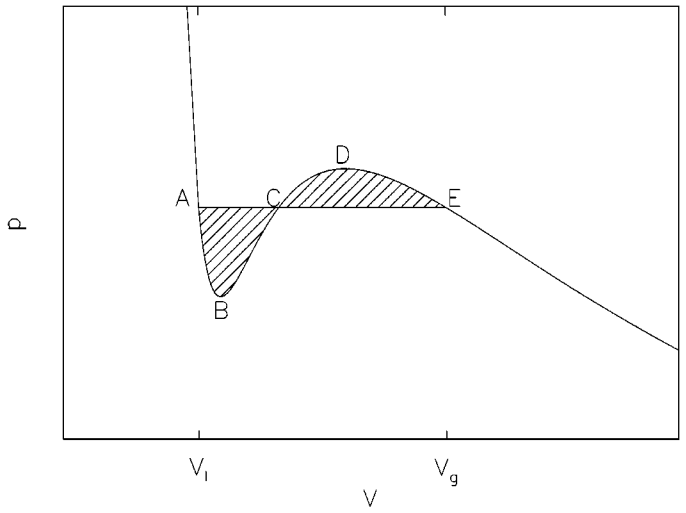

FIG. 1. Illustrative plot of isothermals in phase diagram.

Using the Chapman–Enskog expansion, we can prove that the Boltzmann equation, (1), recovers the macroscopic equations

$$\frac{\partial \rho}{\partial t} + \nabla \cdot (\rho \mathbf{u}) = 0, \tag{15}$$

$$\rho \left[\frac{\partial \mathbf{u}}{\partial t} + (\mathbf{u} \cdot \nabla)\mathbf{u} \right] = -\nabla p + \nabla \cdot \mathbf{\Pi} + \kappa \rho \nabla \nabla^2 \rho + \mathbf{G}, \tag{16}$$

where $\mathbf{\Pi}$ is the viscous stress tensor:

$$\mathbf{\Pi} = \rho \nu (\nabla \mathbf{u} + \mathbf{u} \nabla). \tag{17}$$

The kinetic viscosity ν is related to the relaxation time by $\nu = \lambda RT$. Notice that the above macroscopic momentum equation differs from the Navier–Stokes equation by an additional term, $\kappa \rho \nabla \nabla^2 \rho$. This term contributes exclusively to the surface tension. The above macroscopic equations are consistent with previous results of thermodynamic studies [18].

B. Modification for Incompressible Flow

It is difficult to simulate multiphase flows by directly solving the Boltzmann equation, (1). The difficulty is related to calculation of the intermolecular force. As shown in Eq. (10), the calculation of the intermolecular force involves the evaluation of $\nabla \psi$, which is usually very large along interfaces. (This problem is less substantial for the surface tension term because κ is usually very small.) This difficulty becomes quite substantial for fluids far from the critical point. In this situation, numerical schemes are very unstable under small numerical errors in calculating the intermolecular force.

In this study, we propose to solve this problem by introducing a new variable,

$$g = fRT + \psi(\rho)\Gamma(0), \tag{18}$$

where $\Gamma(\mathbf{u})$ is a function of the macroscopic velocity $\mathbf{u}$:

$$\Gamma(\mathbf{u}) = \frac{1}{(2\pi RT)^{D/2}} \exp\left[-\frac{(\boldsymbol{\xi}-\mathbf{u})^2}{2RT}\right]. \tag{19}$$

It is straightforward to find the evolution equation for g:

$$\frac{Dg}{Dt} = RT\frac{Df}{Dt} + \Gamma(0)\frac{D\psi(\rho)}{Dt}. \tag{20}$$

Since $\psi(\rho)$ is a function of density and for incompressible fluids the material derivative, $d/dt \equiv \partial_t + (\mathbf{u}\cdot\nabla)$, of any function of density is zero, we have

$$\frac{D\psi(\rho)}{Dt} = (\boldsymbol{\xi}-\mathbf{u})\cdot\nabla\psi(\rho). \tag{21}$$

Substituting Eqs. (1), (10) and (21) into Eq. (20), we have

$$\frac{Dg}{Dt} = -\frac{g-g^{\mathrm{eq}}}{\lambda} + (\boldsymbol{\xi}-\mathbf{u})\cdot[\Gamma(\mathbf{u})(\mathbf{F}_s+\mathbf{G}) - (\Gamma(\mathbf{u})-\Gamma(0))\nabla\psi(\rho)], \tag{22}$$

where

$$g^{\mathrm{eq}} = \rho RT\Gamma(\mathbf{u}) + \psi(\rho)\Gamma(0). \tag{23}$$

Through g, we can calculate the pressure and velocity using

$$p = \int g\, d\boldsymbol{\xi}, \tag{24}$$

$$\rho RT\mathbf{u} = \int \boldsymbol{\xi} g\, d\boldsymbol{\xi}. \tag{25}$$

We regard Eq. (22) as computationally superior to Eq. (1) in calculation of the velocity fields. This is because the term involving $\nabla\psi(\rho)$ is now multiplied by a small quantity $\Gamma(\mathbf{u})-\Gamma(0)$. Notice that $\Gamma(\mathbf{u})-\Gamma(0)$ is proportional to $\mathbf{u}/c$ or the Mach number in nearly incompressible limit. Consequently, the effect of the numerical errors in calculation of density gradient is greatly reduced by using Eq. (22).

However, Eq. (22) cannot form a complete set of equations for multiphase flow, because the distribution function g only gives the pressure and velocity. Another important variable in multiphase flow, the density, still remains to be determined. (Notice that the density is not uniquely defined for a given pressure.) For incompressible multiphase flows, the densities of fluids away from the interface are exactly known. The only tasks remaining are to track different phases and to maintain a sharp interface. In this regard, any index function satisfying Eq. (1) can be used for these purposes. Once the index function is known, other physical properties such as density and viscosity can be determined.

The concept of the index function has been used in numerous numerical algorithms of multiphase flow, ranging from the Marker and Cell method [19] to the level set approach [20]. Nevertheless, how to maintain a sharp interface remains a topic of research for the traditional method [21]. In our formulation, incorporation of intermolecular force automatically takes care of this problem.

Now that Eq. (1) is only used for tracking the density field, we can drop the gravity and surface tension forces in Eq. (1), since they have no effect on mass conservation. However, the intermolecular force term, $\nabla\psi(\rho)$, must be retained because it is essential in maintaining a sharp interface between different phases.

In summary, we propose the following formulation to simulate incompressible multiphase flow,

$$\frac{Df}{Dt} = -\frac{f - f^{\mathrm{eq}}}{\lambda} - \frac{(\boldsymbol{\xi} - \mathbf{u}) \cdot \nabla\psi(\phi)}{RT}\Gamma(\mathbf{u}), \tag{26}$$

$$\frac{Dg}{Dt} = -\frac{g - g^{\mathrm{eq}}}{\lambda} + (\boldsymbol{\xi} - \mathbf{u}) \cdot [\Gamma(\mathbf{u})(\mathbf{F}_s + \mathbf{G}) - (\Gamma(\mathbf{u}) - \Gamma(0))\nabla\psi(\rho)], \tag{27}$$

where f is the distribution of the index function, ϕ, and g is the distribution function of pressure. The equilibrium distributions for f and g are

$$f^{\mathrm{eq}} = \phi\Gamma(\mathbf{u}), \tag{28}$$

$$g^{\mathrm{eq}} = \rho RT\Gamma(\mathbf{u}) + \psi(\rho)\Gamma(0), \tag{29}$$

where

$$\Gamma(\mathbf{u}) = \frac{1}{(2\pi RT)^{D/2}} \exp\left[-\frac{(\boldsymbol{\xi} - \mathbf{u})^2}{2RT}\right]. \tag{30}$$

The macroscopic variables are calculated by

$$\phi = \int f \, d\boldsymbol{\xi}, \tag{31}$$

$$p = \int g \, d\boldsymbol{\xi}, \tag{32}$$

$$\rho RT\mathbf{u} = \int \boldsymbol{\xi} g \, d\boldsymbol{\xi}. \tag{33}$$

There are many ways to calculate physical properties, such as the density and viscosity, from the index function. In this study, we choose the formulations

$$\rho(\phi) = \rho_l + \frac{\phi - \phi_l}{\phi_h - \phi_l}(\rho_h - \rho_l), \tag{34}$$

$$\nu(\phi) = \nu_l + \frac{\phi - \phi_l}{\phi_h - \phi_l}(\nu_h - \nu_l), \tag{35}$$

where ρ_l and ρ_h are densities of light and heavy fluids, respectively; ν_l and ν_h are viscosities of light and heavy fluids, respectively; and ϕ_l and ϕ_h are the minimum and maximum values of the index function.

The macroscopic equations for the modified scheme are

$$\frac{1}{\rho RT}\frac{\partial p}{\partial t} + \nabla \cdot \mathbf{u} = 0, \tag{36}$$

$$\rho\left[\frac{\partial \mathbf{u}}{\partial t} + (\mathbf{u} \cdot \nabla)\mathbf{u}\right] = -\nabla p + \nabla \cdot \boldsymbol{\Pi} + \kappa\rho\nabla\nabla^2\rho + \mathbf{G}. \tag{37}$$

In the nearly incompressible limit, the time derivative of the pressure is small and the incompressible condition is approximately satisfied [22]. In a sense, our approach is close to the pseudo-incompressible technique in classical CFD methods [23].

III. LATTICE BOLTZMANN SCHEME FOR MULTIPHASE FLOW IN THE NEARLY INCOMPRESSIBLE LIMIT

In the preceding section, we have proposed a continuous formulation based on distribution functions for simulation of incompressible multiphase flow. Our ultimate goal is to establish a computational scheme which can be run on a digital computer. In this section, we will discretize the continuous equations in Section II to derive a lattice Boltzmann method.

It has been shown [24–26] that the lattice Boltzmann method can be derived by systematically discretizing the continuous Boltzmann equation. There are several steps in this procedure. First, we need to discretize the microscopic velocity space into a set of discrete velocities so that the moment integrals of the distribution functions can be numerically calculated using Gauss–Hermite quadratures. In two dimensions, the following 9-bit model satisfies this requirement [25],

$$\mathbf{e}_\alpha = \begin{cases} \mathbf{0}, & \alpha = 0, \\ (\cos[(\alpha-1)\pi/2],\ \sin[(\alpha-1)\pi/2])c, & \alpha = 1,\ 2,\ 3,\ 4, \\ \sqrt{2}(\cos[(\alpha-5)\pi/2+\pi/4],\ \sin[(\alpha-5)\pi/2+\pi/4])c, & \alpha = 5,\ 6,\ 7,\ 8, \end{cases} \tag{38}$$

where $c = \sqrt{3RT}$. The corresponding discrete distribution functions are consequently defined as

$$f_\alpha(\mathbf{x}, t) = w_\alpha f(\mathbf{x}, \mathbf{e}_a, t), \tag{39}$$

$$g_\alpha(\mathbf{x}, t) = w_\alpha g(\mathbf{x}, \mathbf{e}_a, t), \tag{40}$$

where $w_0 = \frac{4}{9}$, $w_\alpha = \frac{1}{9}$ for $\alpha = 1, 2, 3, 4$, and $w_\alpha = \frac{1}{36}$ for $\alpha = 5, 6, 7, 8$ are integral weights. By Taylor-expanding $\Gamma(\mathbf{u})$ in terms of the Mach number, $\mathbf{u}/\sqrt{RT}$, we obtain the simplified equilibrium distribution functions of f_α and g_α [25]:

$$f_\alpha^{\mathrm{eq}} = w_\alpha \phi \left[1 + \frac{3\mathbf{e}_\alpha \cdot \mathbf{u}}{c^2} + \frac{9(\mathbf{e}_\alpha \cdot \mathbf{u})^2}{2c^4} - \frac{3\mathbf{u}^2}{2c^2}\right], \tag{41}$$

$$g_\alpha^{\mathrm{eq}} = w_\alpha \left[p + \rho\left(\frac{3\mathbf{e}_\alpha \cdot \mathbf{u}}{c^2} + \frac{9(\mathbf{e}_\alpha \cdot \mathbf{u})^2}{2c^4} - \frac{3\mathbf{u}^2}{2c^2}\right)\right]. \tag{42}$$

Second, we need to discretize the continuous equation in temporal space. From our previous studies [9], a second order scheme is required for simulation of multiphase flow. To maintain an explicit scheme, we introduce the variables

$$\bar{f}_\alpha = f_\alpha + \frac{(\mathbf{e}_a - \mathbf{u}) \cdot \nabla\psi(\phi)}{2RT}\Gamma_\alpha(\mathbf{u})\delta_t, \tag{43}$$

$$\bar{g}_\alpha = g_\alpha - \frac{1}{2}(\mathbf{e}_a - \mathbf{u}) \cdot [\Gamma_\alpha(\mathbf{u})(\mathbf{F}_s + \mathbf{G}) - (\Gamma_\alpha(\mathbf{u}) - \Gamma_\alpha(0))\nabla\psi(\rho)]\delta_t, \tag{44}$$

where δ_t is the time-step and

$$\Gamma_\alpha(\mathbf{u}) = w_\alpha\left[1 + \frac{3\mathbf{e}_\alpha \cdot \mathbf{u}}{c^2} + \frac{9(\mathbf{e}_\alpha \cdot \mathbf{u})^2}{2c^4} - \frac{3\mathbf{u}^2}{2c^2}\right]. \tag{45}$$

The newly introduced variables $\bar{f}$ and $\bar{g}$ satisfy the discrete evolution equations

$$\begin{aligned}
&\bar{f}_\alpha(\mathbf{x} + \mathbf{e}_a\delta_t, t + \delta_t) - \bar{f}_\alpha(\mathbf{x}, t) \\
&\quad = -\frac{\bar{f}_\alpha(\mathbf{x}, t) - f_\alpha^{\mathrm{eq}}(\mathbf{x}, t)}{\tau} - \frac{(2\tau - 1)}{2\tau}\frac{(\mathbf{e}_a - \mathbf{u}) \cdot \nabla\psi(\phi)}{RT}\Gamma_\alpha(\mathbf{u})\delta_t, \qquad (46) \\
&\bar{g}_\alpha(\mathbf{x} + \mathbf{e}_a\delta_t, t + \delta_t) - \bar{g}_\alpha(\mathbf{x}, t) \\
&\quad = -\frac{\bar{g}_\alpha(\mathbf{x}, t) - g_\alpha^{\mathrm{eq}}(\mathbf{x}, t)}{\tau} + \frac{2\tau - 1}{2\tau}(\mathbf{e}_a - \mathbf{u}) \cdot [\Gamma_\alpha(\mathbf{u})(\mathbf{F}_s + \mathbf{G}) \\
&\qquad - (\Gamma_\alpha(\mathbf{u}) - \Gamma_\alpha(0))\nabla\psi(\rho)]\delta_t, \qquad (47)
\end{aligned}$$

where $\tau = \lambda/\delta_t$. A third-order differencing scheme was used to calculate $\nabla\psi$. The macroscopic variables can be calculated using

$$\phi = \sum \bar{f}_\alpha, \tag{48}$$

$$p = \sum \bar{g}_\alpha - \frac{1}{2}\mathbf{u} \cdot \nabla\psi(\rho)\delta_t, \tag{49}$$

$$\rho RT\mathbf{u} = \sum \mathbf{e}_a\bar{g}_\alpha + \frac{RT}{2}(\mathbf{F}_s + \mathbf{G})\delta_t. \tag{50}$$

Third, we need to discretize the physical space into a computational grid. For isothermal flows, the computation can be greatly simplified if the physical space can be discretized so that every discrete distribution function travels from one grid node to another one in each time step. In two dimensions, this can be realized by utilizing a regular square lattice with a lattice length of $c\delta_t$.

Equations (46) to (50) construct the lattice Boltzmann scheme for incompressible multiphase flow. In this model, the kinetic viscosity relates to the relaxation parameter by $\nu = (\tau - \frac{1}{2})RT\delta_t$.

IV. NUMERICAL SIMULATION OF RAYLEIGH–TAYLOR INSTABILITY

When a layer of heavy fluid is placed on top of another layer of light fluid in a gravitational field with gravity pointing downward, the initial planar interface is unstable. Any disturbance will grow to produce spikes of heavy fluids moving downward and bubbles of light fluids moving upward. This is the so-called Rayleigh–Taylor instability (for review, see [27]).

In this study, we only focus on the two-dimensional Rayleigh–Taylor instability. The computational domain is a two-dimensional box. Non-slip boundary conditions are applied at the top and bottom walls. Periodic boundary conditions are applied at the side boundaries. The kinetic viscosity is assumed to be the same for both heavy and light fluids. Surface tension is neglected in the simulation. The function $\psi(\phi)$ is chosen so that the pressure satisfies the Carnahan–Starling equation of state in Eq. (14). The parameter a is chosen to be bc^2, which is sufficient to induce phase segregation.

We present our results in terms of non-dimensional variables. Unless otherwise mentioned, we took the channel width W as the length scale and $T = \sqrt{W/g}$ as the time scale, where g is the gravity. The non-dimensional parameters in our studies are the Reynolds number, $\mathrm{Re} = \sqrt{Wg}W/\nu$, and the Atwood number, $A = (\rho_h - \rho_l)/(\rho_h + \rho_l)$, where ρ_h and ρ_l are densities of heavy and light fluids, respectively.

A. Single-Mode

The single-mode Rayleigh–Taylor instability provides a good benchmark for numerical simulations of multiphase flows. In the early stage when the amplitude of the perturbation is much smaller than the wave length, the perturbation of the fluid interface has an exponential growth [28, 29],

$$h = h_0 e^{\alpha t}, \tag{51}$$

where h is the amplitude at time t, h_0 is the initial amplitude, and α is the growth rate of the perturbation. With the kinetic viscosity ratio to be one and the surface tension negligible, the growth rate is a function of Atwood number and wave number $k = 2\pi/W$. Figure 2 plots the growth rate measured in our LBM simulations along with the theoretical prediction by Chandrasekhar [29] at three different Atwood numbers, $A = 0.2$, 0.5, and 0.8. The simulations were carried out on a 64×128 grid. The growth rate is measured in units of $(g^2/\nu)^{1/3}$ and the wave number is measured in units of $(g/\nu^2)^{1/3}$. As shown, our growth rates agree well with the theoretical results. The minor discrepancy may be due to the limited grid size.

The single-mode Rayleigh–Taylor instability exhibits a much more complicated pattern at large amplitudes. Figure 3 shows the evolution of the fluid interface from a 10% initial

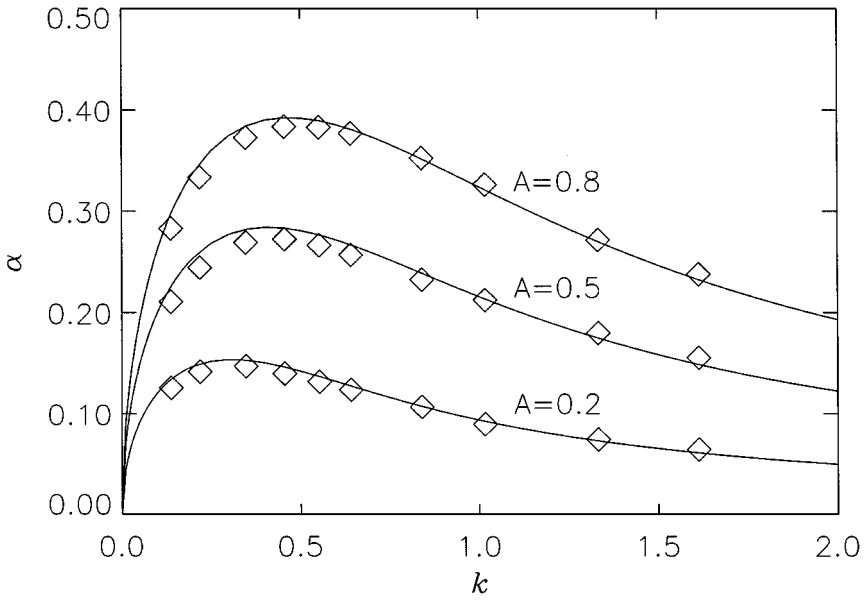

FIG. 2. The dependence of the linear growth rate, α (measured in units of $(g^2/\nu)^{1/3}$), of a disturbance on its wavenumber, k (measured in units of $(g/\nu^2)^{1/3}$), for three different Atwood numbers. The symbol is for numerical simulation and the solid line is for the theoretical results by Chandrasekhar.

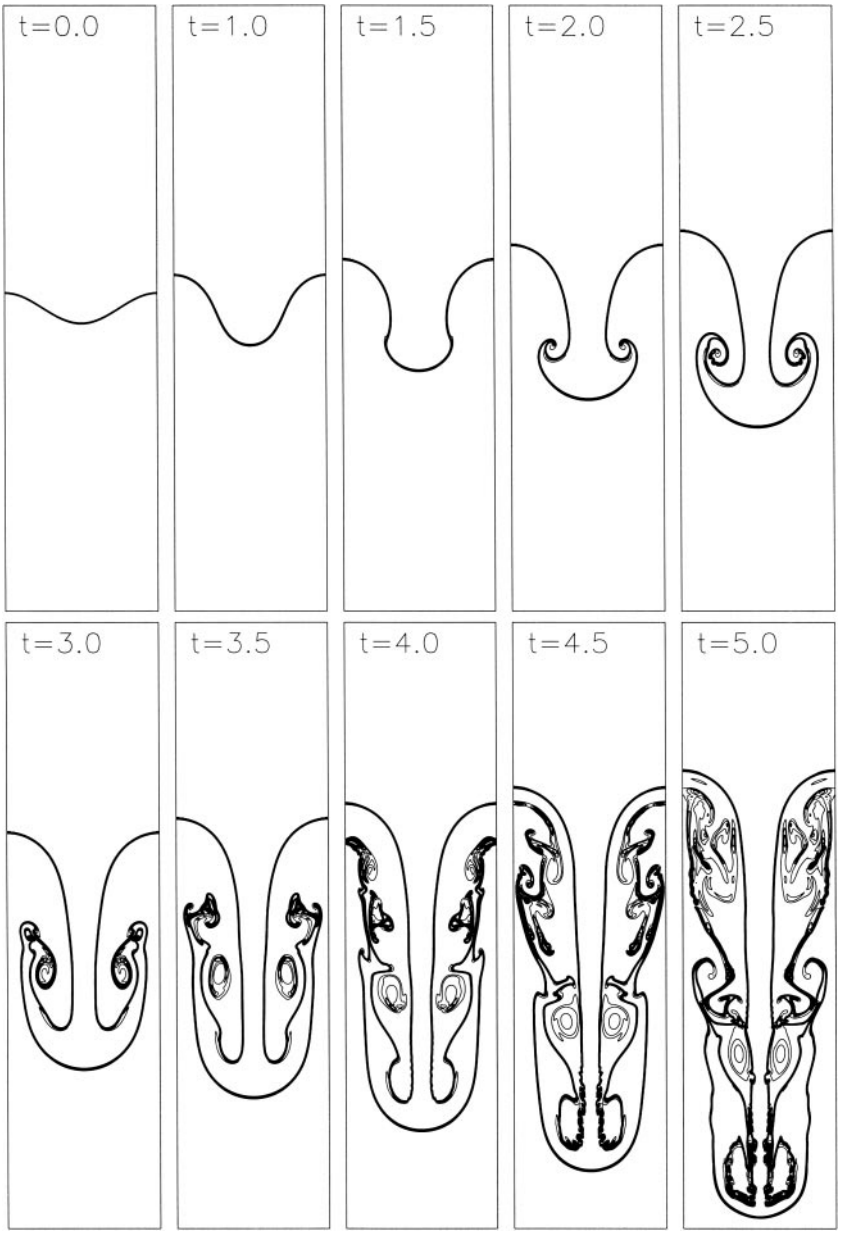

FIG. 3. Evolution of the fluid interface from a single mode perturbation. The Atwood number is 0.5 and the Reynolds number is 2048. A total of 19 density contours are plotted. The time is measured in units of $\sqrt{W/g}$.

perturbation. The Atwood number is 0.5 and the Reynolds number is 2048. The simulation was carried out on a 256×1024 grid. The gravity was chosen so that $\sqrt{Wg} = 0.04$. The interface was represented by 19 equally spaced density contours. During the early stages ($t < 1.0$), the growth of the fluid interface remains symmetrical up-and-down. Later, the heavy fluid falls as a spike and the light fluid rises to form bubbles. Starting from $t = 2.0$, the heavy fluid begins to roll up into two counter-rotating vortices. This phenomenon was first computed by Daly [30] and studied further by other authors [31–34]. At a later time ($t = 3.0$), these two vortices become unstable and a pair of secondary vortices appear at

the tails of the roll-ups. The roll-ups and vortices in the heavy fluid spike are due to the Kelvin–Helmholtz instability [30]. The shapes of the fluid interface in the current study compare well with those in previous studies [30, 33].

We continue our simulation to later time ($t = 5.0$). With an increase in time, the heavy fluid falling down gradually forms one central spike and two side spikes. It is interesting to note that only the side spikes of the heavy fluid experience the Kelvin–Helmholtz instability and the interfaces along these two spikes are stretched and folded into very complicated shapes. The mixing of heavy and light fluids is significant. On the other hand, the interface along the central spike, as well as the fronts of both bubble and spike, remains relatively smooth.

The features of Rayleigh–Taylor instability in the late stage can be better illustrated via the velocity fields. In Fig. 4, we plotted the contours of streamlines at the left side panel

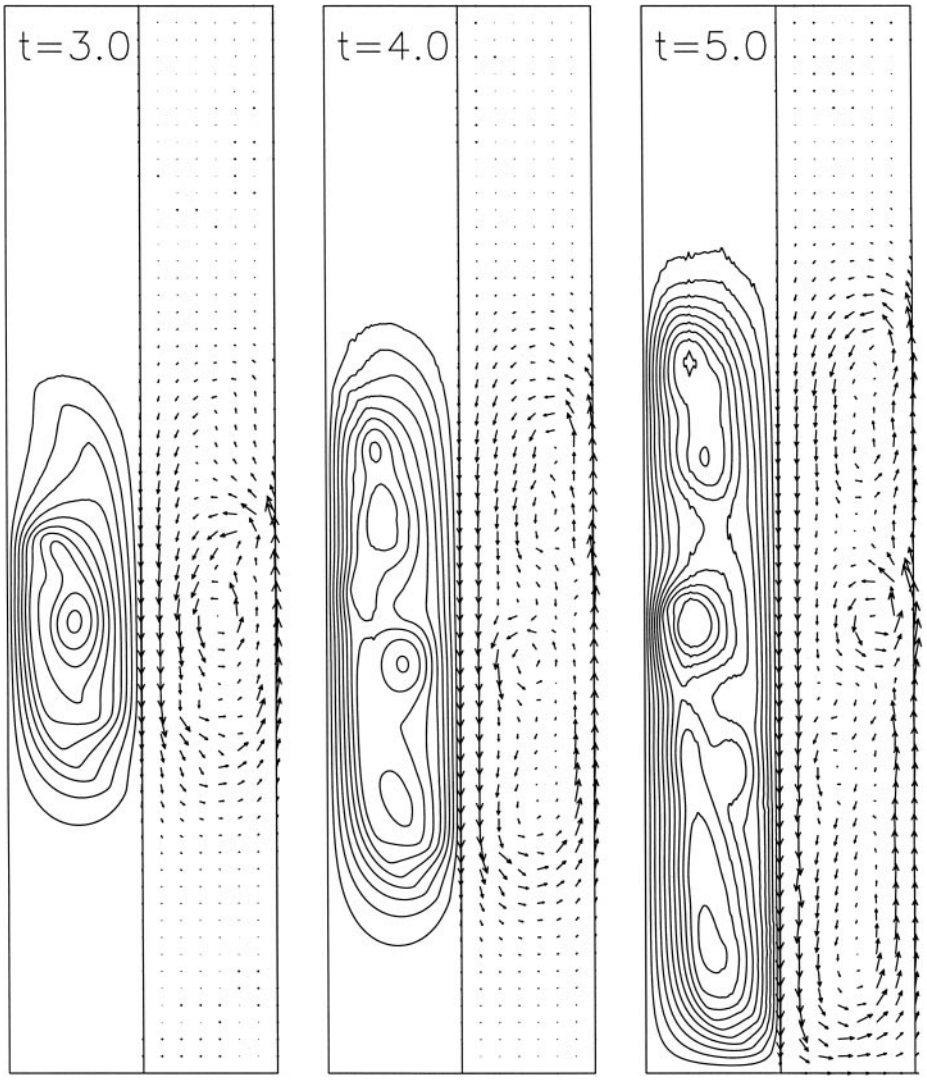

FIG. 4. Velocity fields of the Rayleigh–Taylor instability at a late stage. The left panels are the streamlines and the right panels are the velocity vectors. The streamline is measured in units of $\sqrt{W/g}W$ and the interval between contours is 0.02.

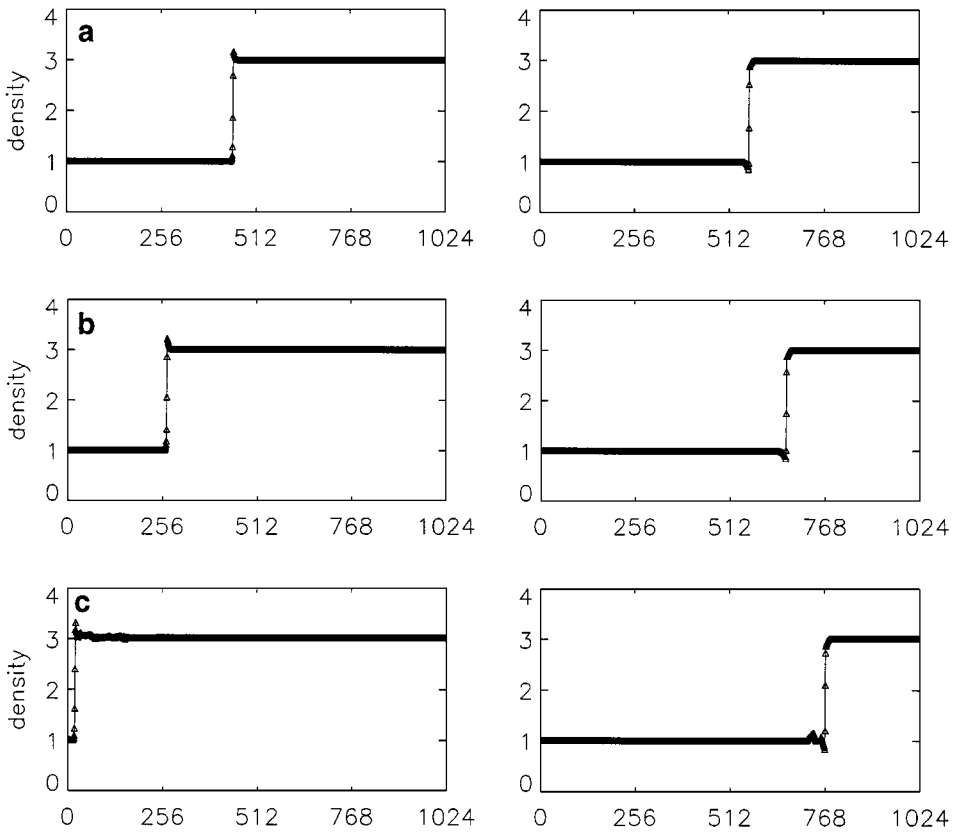

FIG. 5. Density profiles across the bubble and spike fronts at three different time steps, (a) $t = 1.0$, (b) $t = 3.0$, and (c) $t = 5.0$. The horizontal axis is the computational grid. The left panel shows the interface across the spike and the right panel shows the interface across the bubble. The Atwood number is 0.5 and the Reynolds number is 2048.

and the velocity vector plots at the right side panel. As expected, the heavy fluid falls down in the middle and the light fluid rises along the edges. Between them exists a strong shear layer–a condition that incubates Kelvin–Helmholtz instability. A distorted single vortex is clearly visible at $t = 3.0$. With an increase in time, more and more vortices are generated and the flow field becomes quite distorted along the quadrants of the channel. This flow pattern is consistent with the distortion of the interface along the side spikes.

One of the advantages of our LBM multiphase scheme is that the fluid interface does not diffuse in simulations. Figure 5 shows the density profiles across the spike and bubble fronts in the above run. As shown, the interface remains sharp throughout the simulation. No special treatment is used to reconstruct the interface. The interface thickness takes about 3–4 grid spacings. There exist some "jiggles" near the interface and their causes need more study.

To study the effect of the viscosity on Rayleigh–Taylor instability, we repeated the above simulation using the same parameters except for decreasing the Reynolds number to 256. Figure 6 shows the time evolution of the fluid interface. Compared to those in Fig. 3, the shapes of the bubble and spike fronts are almost the same. However, a decrease in Reynolds number (or an increase in viscosity) significantly suppresses the development of Kelvin–Helmholtz instability. Although the heavy fluid still rolls up as two side spikes, the interface

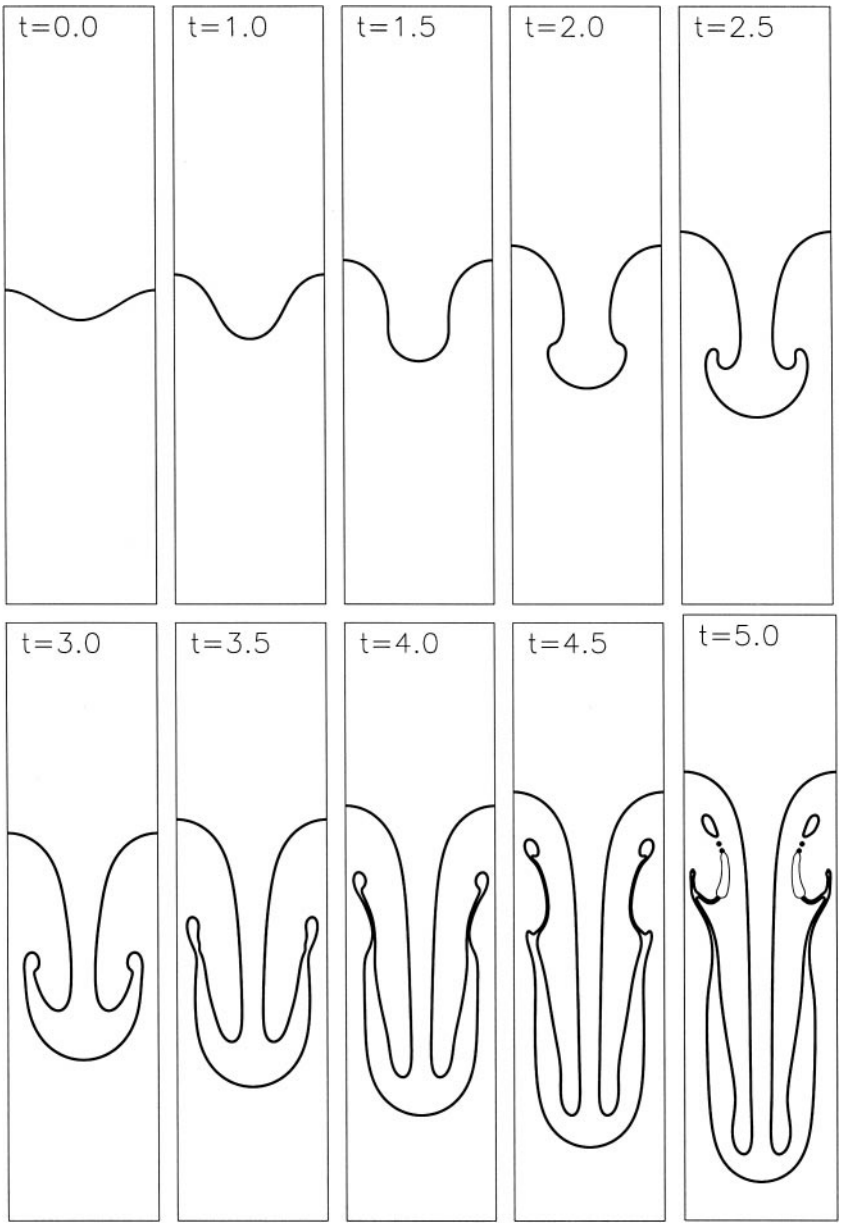

FIG. 6. Evolution of the fluid interface from a single mode perturbation. The Atwood number is 0.5 and the Reynolds number is 256. A total of 19 density contours are plotted. The time is measured in units of $\sqrt{W/g}$.

along the side spikes remains rather smooth. The spiral vortices shown in Fig. 3 are not observed.

In Fig. 7, we plot the positions and velocities of the bubble front and spike tip versus time for the runs in Figs. 3 and 6. After an early stage ($t < 1.0$), the bubble settles into a cruising state. The bubble movement shows little dependence on the Reynolds number. The terminal bubble velocity, measured in units of $\sqrt{AgW}$, is 0.270. This result compares well with the value of 0.265 obtained by Tryggvason using a front-tracking approach [33]. Note that in Tryggvason's study, the viscosity was neglected. The growth of the spike shows a

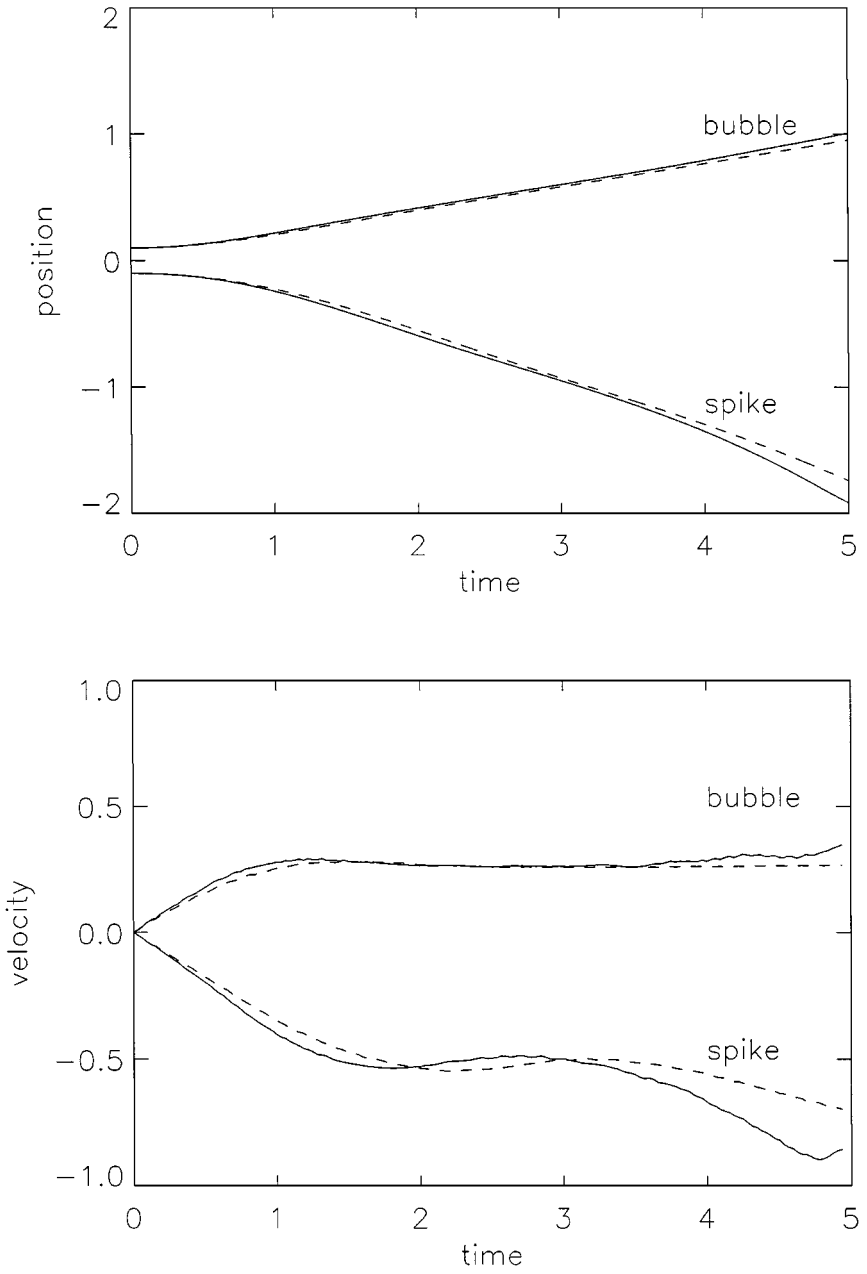

FIG. 7. Positions and velocities of the bubble and spike fronts versus time. The Atwood number is 0.5. The solid lines are from simulation at Re = 2048, while the dashed lines are from simulation at Re = 256. The length is measured in units of W and the time is measured in units of $\sqrt{W/g}$.

more complicated pattern. After an early-stage acceleration, for $t > 1.0$, the spike slows down a little and accelerates again. This re-acceleration starts earlier and appears stronger at the higher Reynolds number (Re = 2048) than at the lower Reynolds number (Re = 256). Because the only noticeable difference between the Rayleigh–Taylor instabilities at high Reynolds number and at low Reynolds number is the appearance of the secondary vortices, we suspect the re-acceleration of the spike may be due to the interaction among the secondary

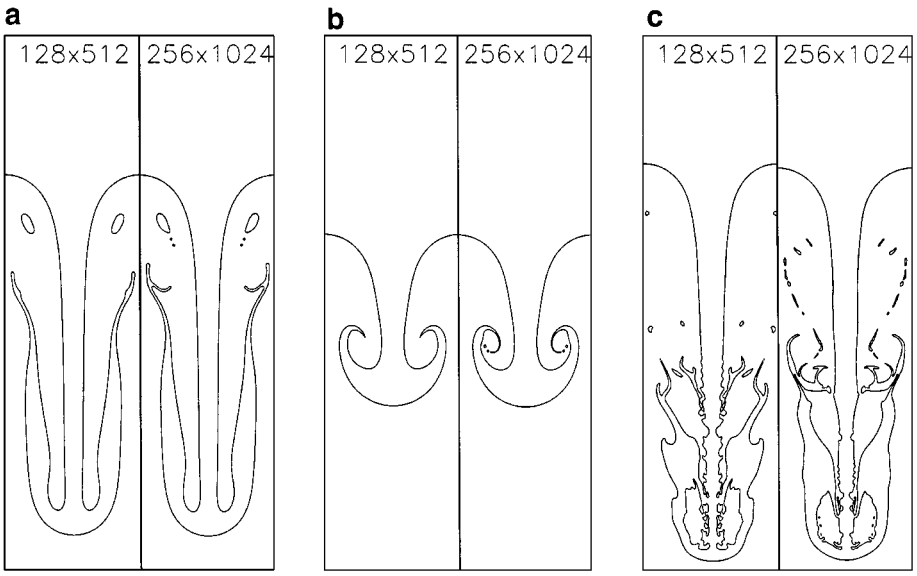

FIG. 8. Grid convergence of numerical solutions, (a) $\mathrm{Re} = 256$, $t = 5.0$, (b) $\mathrm{Re} = 2048$, $t = 2.5$, and (c) $\mathrm{Re} = 2048$, $t = 5.0$. Only the contour of $0.5(\rho_\mathrm{i} + \rho_\mathrm{h})$ is plotted. The Atwood number is 0.5.

vortices. The sharp drop in the spike velocity at the end of the run is due to the boundary effect of the bottom wall.

One of the important issues in numerical simulations of Rayleigh–Taylor instability is the grid convergence of solutions. It has been observed by several authors [33, 34] that numerical solutions do not converge under grid refinement when the viscosity is totally neglected. It was argued [35, 33] that this lack of convergence is due to the formation of a singularity on vortex sheet at the center of the roll-up. This singularity should be removed when the viscosity exists. Figure 8 shows the grid dependence of our solutions. At $\mathrm{Re} = 256$ (Fig. 8a), our solution is almost converged up to $t = 5.0$ except a small protrusion near the tails of the side spikes. At a larger Reynolds number of 2048 (Fig. 8b), the basic structures of the bubble and spike up to $t = 2.5$ are well converged but the details in the vortices still have differences. On the fine grid (256×1024), the thickness of the thin filaments in the roll-up vortices is measured to be 6–8 grid spacings. Considering that the interface in our scheme takes 3–4 grid spacings, it is reasonable that the coarse grid (128×512) cannot reveal these thin filaments. However, our solution at $\mathrm{Re} = 2048$ does not converge at $t = 5.0$ although the bubble front and spike tip show little dependence on grid size. How the grid convergence varies with Reynolds number needs more study.

To study the effect of the Atwood number, we also carried out simulations of the Rayleigh–Taylor instability for an Atwood of 0.9. The Reynolds number is chosen to be 614.4 in this case. Figure 9 shows the evolution of the fluid interface from an initial 10% perturbation in amplitude. Compared this with the case of $A = 0.5$, the instability grows much faster. The roll-ups of the heavy fluid still show up but this happens at a much larger amplitude. Obviously, Kelvin–Helmholtz instability becomes less important in Rayleigh–Taylor instability at high Atwood numbers. The terminal bubble velocity, measured in units of $\sqrt{AgW}$, is 0.275 in this case.

It is interesting to compare our simulation results with those using the LBM multiphase model of Gunstensen *et al.* [36]. Although both models successfully predicted the linear

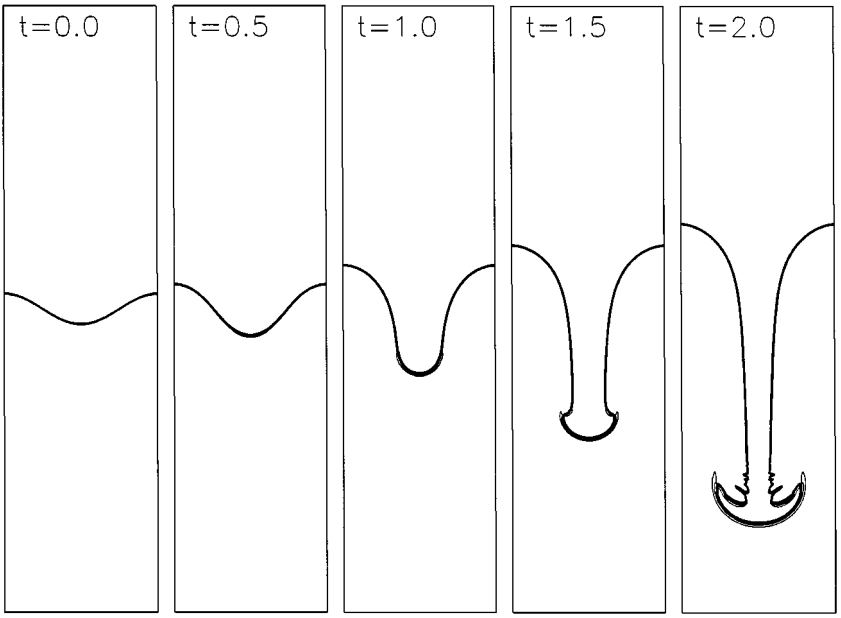

FIG. 9. Evolution of the fluid interface from a single mode perturbation. The Atwood number is 0.9 and the Reynolds number is 614.4. A total of 19 density contours are plotted. The time is measured in units of $\sqrt{W/g}$.

growth rate at the initial stage, the present scheme did a much better job in capturing the interface evolution at late stages. The vortex roll-up, which was not resolved in [36], was successfully simulated in the present study.

B. Multiple Mode

Although the single-mode Rayleigh–Taylor instability is a good example for benchmark studies and has many interesting phenomena to explore, in real situations the instability will likely grow from an initial perturbation with multiple wavelengths. This type of Rayleigh–Taylor instability eventually evolves into turbulent mixing. Direct numerical simulation is useful in understanding this complicated process.

We carried out our simulations of multiple-mode Rayleigh–Taylor instability on a 512×512 grid. The Reynolds number was chosen to be 4096 and the Atwood number was fixed at 0.5. The gravity was chosen so that $\sqrt{Wg} = 0.08$. The initial perturbation of the fluid interface was given by

$$h = \sum_n a_n \cos(k_n x) + b_n \sin(k_n x), \tag{52}$$

where $k_n = 2n\pi / W$ is the wave number. The amplitudes, a_n and b_n, were randomly chosen from a Gaussian distribution. A total of 10 modes ($n \in [21, 30]$) were used.

The evolution of a multiple-mode Rayleigh–Taylor instability is shown in Fig. 10 at six time steps. The early stage ($t < 1.0$) was characterized with growth of structures with small wave numbers. The heavy fluid falls down as slender spikes while the light fluid rises up as small bubbles. The amplitudes of perturbations have grown much larger than the initial wavelength at $t = 1.0$. The interaction among small structures becomes obvious at $t = 2.0$

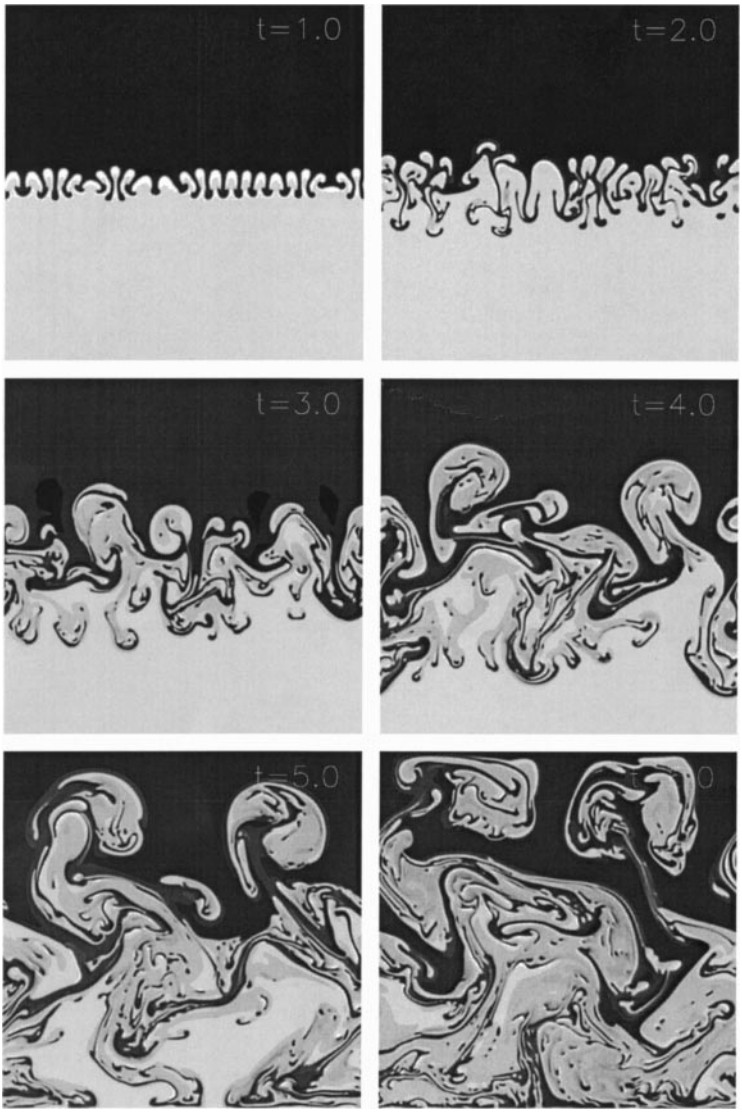

FIG. 10. Rayleigh–Taylor instability from a multiple mode perturbation. The Atwood number is 0.5 and the Reynolds number is 4096. The time is measured in units of $\sqrt{W/g}$.

and continues throughout the simulation. Three features can be observed during this stage. First, the larger bubbles rise faster than smaller ones. This is because the bubble at this stage moves in proportional to its size. Second, small bubbles continue to merge into larger ones. At the time of $t = 4.0$, the initial perturbation totally disappeared and the dominant wavelength becomes $W/2$. Notice that this long wavelength does not exist in the initial perturbation. Third, the interaction among bubbles leads to a turbulent mixing layer. The thickness of this mixing layer increases with time.

To quantify the characteristics of the turbulent mixing layer, we plotted in Fig. 11 the averaged density profile against depth. The average density in the mixing layer is defined as

$$\bar{\rho}(z) = \int \rho(x, z)\, dx. \tag{53}$$

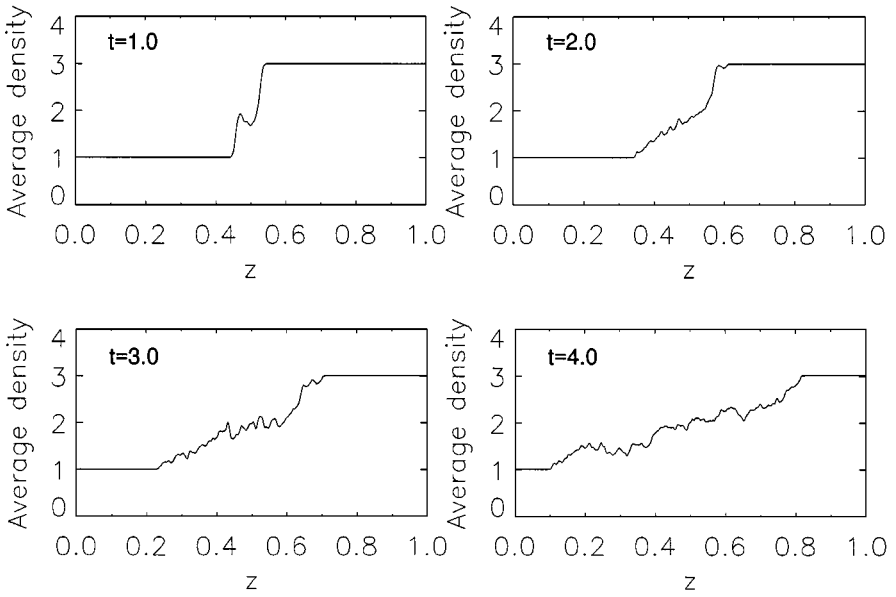

FIG. 11. Fluid density averaged over horizontal layers plotted against depth in a multiple-mode Rayleigh–Taylor instability.

The averaged density profiles have similar shapes while the thickness of the mixing layer increases with time. There are zig-zags in the density profiles which indicate the irregularity in the mixing layer. Figure 12 plots the bubble and spike fronts of the mixing layer against time, where the bubble front, h_1, and the spike front, h_2, are defined

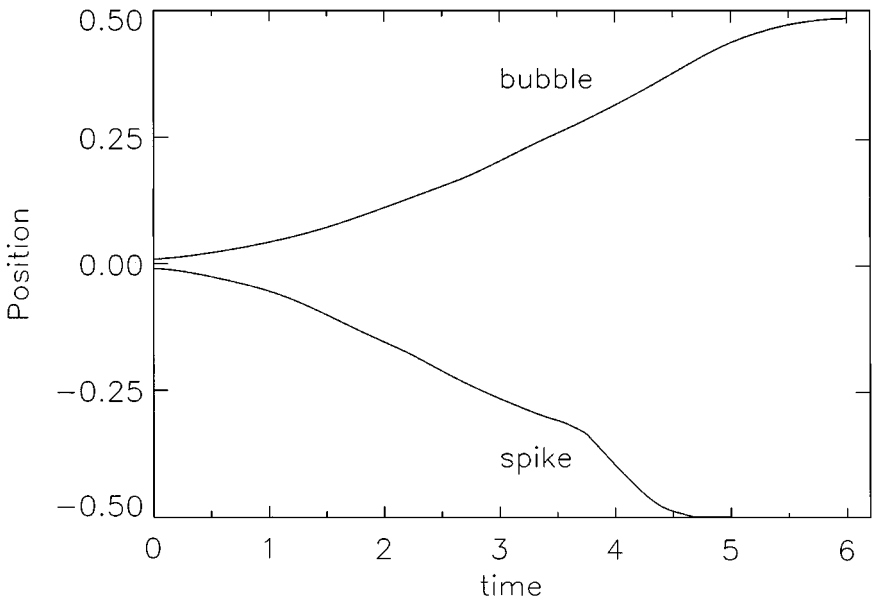

FIG. 12. Positions of the bubble and spike envelope versus time. The Atwood number is 0.5 and the Reynolds number is 4096. The length is measured in units of W and the time is measured in units of $\sqrt{W/g}$.

as

$$\bar{\rho}(h_1) - \rho_l = 0.99(\rho_h - \rho_l),$$
$$\bar{\rho}(h_2) - \rho_l = 0.01(\rho_h - \rho_l).$$

Previous studies [31, 37, 38] have shown that the bubble front grows as $h = \alpha Agt^2$ after an initial stage. Our results show the same trend. The non-dimensional coefficient α measured from our simulation is 0.04, which is at the lower bound of the range 0.04–0.05 reported by Youngs [31, 38].

V. CONCLUSIONS AND DISCUSSIONS

We have proposed a lattice Boltzmann scheme for simulation of incompressible multiphase flow. Unlike traditional CFD approaches which solve macroscopic governing equations, our scheme is based on the mesoscopic kinetic equation. The phase segregation and interfacial dynamics are modeled by incorporation of molecular interactions. The sharp interface between different phases can be automatically maintained without any artificial treatments. For the incompressible flow, we use two sets of distribution functions: one for tracking the pressure and velocity fields and the other for the density field. Using the distribution function of pressure enables us to reduce substantially the effect of numerical errors in calculation of intermolecular force.

Numerical simulations were carried out for the two-dimensional Rayleigh–Taylor instability developed from both single-mode and multiple-mode initial perturbations. Our simulations reveal most features of Rayleigh–Taylor instability observed in previous theoretical and numerical studies. For the single-mode Rayleigh–Taylor instability, both the initial linear growth rate and the terminal bubble velocity agree well quantitatively with the theoretical prediction and previous numerical simulations. For the multiple-mode Rayleigh–Taylor instability, the growth of the mixing layer compares well with other studies.

Our study also reveals several new aspects of the physics of the single-mode Rayleigh–Taylor instability. First, at the very late stage, the spike starts a reaccelaration phase, probably due to the growth of Kelvin–Helmholtz instability in the wake of the main spike. Second, the viscosity has little effect on the evolutions of the bubble and main spike, but it affects the growth of Kelvin–Helmholtz instability.

The modification for the nearly incompressible limit in this paper may not preserve the mesoscopic physics, such as the interface shape. It nevertheless works well for studying macroscopic flows where the interface shape is not important. To reveal mesoscopic physics, one must use the original kinetic equation for dense fluids. It should be pointed out that the kinetic-theory-based formulation is not the only one suitable for simulation of multiphase flow. For example, one can solve directly the macroscopic equations, such as those given in Eqs. (15) and (16). However, the kinetic-theory-based formulation provides a natural way to incorporate the microscopic molecular interaction which is the physical origin of all interfacial dynamics. Interfacial dynamics such as phase segregation and surface tension, which are difficult to treat in traditional methods, can be easily modeled in the kinetic-theory-based formulations.

REFERENCES

1. U. Frisch, B. Hasslacher, and Y. Pomeau, Lattice-gas automata for the Navier–Stokes equations, *Phys. Rev. Lett.* **56**, 1505 (1986).

2. D. H. Rothman and S. Zaleski, Lattice-gas models of phase separation: Interface, phase transitions and multiphase flow, *Rev. Mod. Phys.* **66**, 1417 (1994).
3. S. Chen and G. D. Doolen, Lattice Boltzmann method for fluid flows, *Annu. Rev. Fluid Mech.* **30**, 329 (1998).
4. A. K. Gunstensen, D. H. Rothman, S. Zaleski, and G. Zanetti, Lattice Boltzmann model of immiscible fluids, *Phys. Rev. A* **43**, 4320 (1991).
5. D. H. Rothman and J. M. Keller, Immiscible cellular-automaton fluids, *J. Stat. Phys.* **52**, 1119 (1988).
6. D. Grunau, S. Chen, and K. Eggert, A lattice Boltzmann model for multiphase fluid flows, *Phys. Fluids A* **5**, 2557 (1993).
7. X. Shan and H. Chen, Lattice Boltzmann model for simulating flows with multiple phases and components, *Phys. Rev. E* **47**, 1815 (1993).
8. M. R. Swift, W. R. Osborn, and J. M. Yeomans, Lattice Boltzmann simulation of non-ideal fluids, *Phys. Rev. Lett.* **75**, 830 (1995).
9. X. He, X. Shan, and G. D. Doolen, A discrete Boltzmann equation model for non-ideal gases, *Phys. Rev. E* **57**, R13 (1998).
10. X. Shan and H. Chen, Simulation of non-ideal gases and liquid–gas phase transitions by the lattice Boltzmann equation, *Phys. Rev. E* **49**, 2941 (1994).
11. F. J. Alexander, S. Chen, and D. W. Grunau, Hydrodynamic spinodal decomposition: Growth kinetics and scaling functions, *Phys. Rev. B* **48**, 634 (1993).
12. W. R. Osborn, E. Orlandini, M. R. Swift, *et al.*, Lattice Boltzmann study of hydrodynamic spinodal decomposition, *Phys. Rev. Lett.* **75**, 4031 (1995).
13. N. S. Martys and H. Chen, Simulation of multicomponent fluids in complex three-dimensional geometries by the lattice Boltzmann method, *Phys. Rev. E* **53**, 743 (1996).
14. P. L. Bhatnagar, E. P. Gross, and M. Krook, A model for collision process in gases. I. Small amplitude processes in charged and neutral one-component system, *Phys. Rev.* **94**, 511 (1954).
15. J. S. Rowlinson and B. Widom, *Molecular Theory of Capillarity*, Oxford Univ. Press, Oxford, 1982.
16. S. Chapman and T. G. Cowling, *The Mathematical Theory of Non-uniform Gases*, 3rd ed., Cambridge Math. Library, 1970.
17. N. F. Carnahan and K. E. Starling, Equation of state for nonattracting rigid spheres, *J. Chem. Phys.* **51**, 635 (1969)
18. R. Evans, The nature of the liquid–vapor interface and other topics in the statistical mechanics of non-uniform, classical fluids, *Adv. in Phys.* **28**, 143 (1979).
19. C. W. Hirt and B. D. Nichols, Volume of fluids (VOF) method for the dynamics of free boundaries, *J. Comput. Phys.* **39**, 201 (1981).
20. S. Osher and J. A. Sethian, Front propagating with curvature-dependent speed: Algorithm based on Hamilton–Jacobi formulations, *J. Comput. Phys.* **79**, 12 (1988).
21. H. Haj-Hariri, Q. Shi, and A. Borhan, Effect of local property smearing on global variables: Implication for numerical simulations of multiphase flows, *Phys. Fluids* **6**, 2556 (1994).
22. X. He and L. Luo, Lattice Boltzmann model for the incompressible Navier-Stokes equation, *J. Stat. Phys.* **88**, 927 (1997).
23. A. J. Chorin, A numerical method for solving incompressible viscous flow problems, *J. Comput. Phys.* **2**, 12 (1967).
24. X. He and L. Luo, A priori derivation of the lattice Boltzmann equation, *Phys. Rev. E* **55**, R6333 (1997).
25. X. He and L. Luo, On the theory of the lattice Boltzmann method: From the Boltzmann equation to the lattice Boltzmann equation, *Phys. Rev. E* **56**, 6811 (1997).
26. T. Abe, Derivation of the lattice Boltzmann method by means of the discrete ordinate method for the Boltzmann equation, *J. Comput. Phys.* **131**, 241 (1997).
27. D. H. Sharp, An overview of Rayleigh–Taylor instability, *Physica D* **12**, 3 (1984).
28. G. I. Taylor, The instability of liquid surfaces when accelerated in a direction perpendicular to their planes, I, *Proc. R. Soc. London A* **201**, 192 (1950).

29. S. Chandrasekhar, The character of the equilibrium of an incompressible heavy viscous fluid of variable density, *Proc. Camb. Phil. Soc.* **51**, 162 (1955).
30. B. J. Daly, Numerical study of two fluid Rayleigh–Taylor instabilities, *Phys. Fluids* **10**, 297 (1967).
31. D. L. Youngs, Numerical simulation of turbulent mixing by Rayleigh–Taylor instability, *Physica D* **12**, 32 (1984).
32. J. Glimm, G. McBryan, R. Menikoff, and D. H. Sharp, Front-tracking applied to Rayleigh–Taylor instability, *SIAM J. Sci. Stat. Comput.* **7**, 230 (1986).
33. G. Tryggvason, Numerical simulation of the Rayleigh–Taylor instability, *J. Comput. Phys.* **75**, 253 (1988).
34. W. Mulder, S. Osher, and J. A. Sethian, Computing interface motion in compressible gas dynamics, *J. Comput. Phys.* **100**, 449 (1992).
35. D. I. Meiron, G. R. Baker, and S. A. Orszag, Analytic structure of vortex sheet dynamics. I. Kelvin–Helmholtz instability, *J. Fluid Mech.* **114**, 283 (1982).
36. X. Nie, Y. Qian, S. Chen, and G. D. Doolen, Lattice Boltzmann simulation of the two-dimensional Rayleigh–Taylor instability, *Phys. Rev. E* **58**, 6861 (1998).
37. K. I. Read, Experimental investigation on turbulent mixing by Rayleigh–Taylor instability, *Physica D* **12**, 45 (1984).
38. D. L. Youngs, Modelling turbulent mixing by Rayleigh–Taylor instability, *Physica D* **37**, 270 (1989).